Tuning Thermally Treated Graphitic Carbon Nitride for H_2 Evolution and CO_2 Photo-Reduction: The Effects of Materials Properties and Mid-Gap States

Elton M. Dias[†], Konstantinos C. Christoforidis[†,¶], Laia Francàs[‡] and Camille Petit[†,*]

[†]Barrer Centre, Department of Chemical Engineering,
Imperial College London, South Kensington Campus, London SW7 2AZ, UK

[‡]Department of Chemistry, Imperial College London,
South Kensington Campus, London SW7 2AZ, UK

[¶]Current address, Department of Environmental Engineering,
Democritus University of Thrace, Xanthi, Greece

[*]E-mail: camille.petit@imperial.ac.uk, Phone: +44 (0)20 7594 3182

Graphitic carbon nitride (g-C_3N_4) is regarded as an attractive photocatalyst for solar fuels production, i.e. H_2 evolution and CO_2 photo-reduction. Yet, its structural, chemical and optoelectronic properties are very much dependent on the synthesis method and are likely to contribute differently whether H_2 evolution or CO_2 reduction is considered. Little is known about this aspect making it difficult to tailor g-C_3N_4 structure and chemistry for a specific photo-reaction. Herein, we create g-C_3N_4 of varying chemical, structural and optical features by applying specific thermal treat-

ments and investigating the effects of the materials properties on solar fuel production. The samples were characterized across scales using spectroscopic, analytical and imaging tools, with particular attention given to the analyses of trap states. In the case of H_2 evolution, the reaction is controlled by light absorption and charge separation enabled by the presence of trap states created by N vacancies. In the case of CO_2 photo-reduction, reactant adsorption appears as a dominating factor. The analyzes also suggest the thermal treatment leads to the formation of trap states located close to the valence band of g-C_3N_4.

Keywords: g-C_3N_4, H_2 evolution, CO_2 photo-reduction, optoelectronic properties, solar fuels, photocatalysis.

1 Introduction

The field of solar fuels, i.e. the production of fuels using sunlight, provides one of the possible approaches towards energy sustainability.[1,2] Solar fuels reactions include both H_2 evolution, either from direct water splitting[3] or through the use of sacrificial agents,[4] and CO_2 conversion to energy dense compounds, such as CO, HCO_2H or CH_4.[5] This potential energy production route comes with a number of challenges to make such processes efficient, durable and cost effective. In particular, a crucial aspect is the design, production and usage of a photocatalyst. From a fundamental perspective, if the energy levels of a semiconductor (i.e. the positions of the valence and conduction bands) are thermodynamically favorable, a material would be able to promote both the aforementioned reactions mainly depending on the available species on its surroundings. Moreover, the kinetics

of the process will ultimately control the reaction rates and even determine if a reaction takes place or not. If both conditions are satisfied, a photocatalyst could interact with its chemical environment and promote specific reactions in accordance.

To this day, titania – and modifications thereof – remains the benchmark photocatalyst for both H_2 evolution and CO_2 conversion as it allows for a reasonable compromise between efficiency, cost and robustness.[6–8] Yet, the wide band gap and related poor light absorption of titania – only UV radiation is used – constitute a major bottleneck to the deployment of solar fuel technologies. For this reason, a number of other photocatalysts are being explored. These include: metal oxides,[9] chalcogenides,[10] graphene oxide composites,[11] supported plasmonic noble metals,[12–15] metal-organic frameworks,[16,17] graphitic carbon nitride (g-C_3N_4)[18] and composites thereof.[19,20]

Of particular interest here is g-C_3N_4, whose combination of features – i.e. tunable chemistry, metal-free sensitizer nature, visible-light absorption, thermal stability and straightforward synthesis – have made it a strong contestant as a solar fuel photocatalyst. g-C_3N_4 is a 2D polymer chemically composed of C and N, arranged in triazine or tri-s-triazine units.[21] Importantly though, its photocatalytic performance is largely hindered due to fast charge recombination, resulting in low efficiencies.[22–24] Modifications of g-C_3N_4 have been tested in order to improve its photo-activity and efficiency. Some successful attempts include mesostructure introduction,[25] nanostructure engineering,[26,27] co-polymerization,[28] formation of g-C_3N_4 composites,[20,29] noble metal deposition[18] and metal[30]/non-metal doping.[31]

An effective way to tune the g-C_3N_4's light absorption property is to alter the structure and chemistry of the material via a thermal treatment (up to $750\,^{\circ}C$).[32–36] While some have explored synthesizing g-C_3N_4 materials at different temperatures,[32,36] others have employed a post-synthetic thermal treatment in order to modify the bulk g-C_3N_4.[33–35]

The thermal treatment typically leads to a change in the chemistry and structure of the material with appearance of N vacancies and alteration of the 2D stacking and interlayer hydrogen bonding.[33,34] Interestingly, the exact nature of the structural changes seems to vary from study to study and/or is interpreted differently. Regarding the impact of the thermal treatment on the optoelectronic properties, most papers – with the exception of the study by Lin et al.[36] – point to a red-shift on the g-C_3N_4 band gap, due to the activation of electronic transitions from the lone pair of electrons in nitrogen atoms.[32–35] A reduction of charge recombination has been observed across the different works.[32–36] The creation of mid-gap states has been speculated in order to explain the trends observed in terms of H_2 evolution and/or CO_2 production.[34,35] From these prior studies, it is clear that thermal treatment has a positive impact on the light absorption property of the materials and its photocatalytic performance. However, the reason for such improvement remains loosely understood and therefore controlled. Particularly, the position of the trap-states created upon thermal treatment has not been clarified. Yet, this has a direct impact on the possible reactions to be catalyzed. In addition, the role of the materials properties – be it chemical, structural or optoelectronic – are likely to vary whether H_2 evolution or CO_2 photo-reduction is considered, especially when, in the latter case, gas phase reactions take place. Understanding the requirements in terms of materials features for these reactions is crucial for the design of improved photocatalysts. This has never been reported before and has direct impact in the design of carbon nitride based photocatalytic structures for solar fuel production. In fact, the two reactions investigated herein are in competition and are scarcely presented in a single work in the literature, specially using carbon nitride materials.

This study focuses on precisely exploiting thermal treatment to create a range of carbon nitride materials with varied chemistry and structure. These materials are used

to link the materials features – structural, chemical and optoelectronic (particularly mid-gap states creation) – to both H_2 evolution and CO_2 photo-reduction performances. As part of this 'exercise', we investigated the position of mid-gap states. To conduct this overall study, detailed profiles of the materials band structure as well as chemical and physical properties were built using a range of complementary analytical, imaging and spectroscopic techniques.

2 Experimental

2.1 Materials and reagents

Ethanol (99.9 %) and sodium sulfate used for electrolyte preparation were purchased from VWR. Reactants melamine (99 %) and triethanolamine (99.0 %) (TEOA) were obtained from Sigma-Aldrich. The resin used in the electrodes preparation was a tropicalized varnish RS 199-1496. All chemicals were used as received without further purification.

2.2 g-C_3N_4 synthesis and thermal treatment

g-C_3N_4 was synthesized by adding melamine to a covered ceramic crucible. The crucible was then heated at 5 °C min^{-1} up to 560 °C under static air. The temperature was maintained for 4 h and the sample was finally let to naturally cool-down. The as-synthesized bulk g-C_3N_4 product was labeled as 'CN-as'. This sample was then subjected to further thermal treatment. In a typical experiment, 1.8 g of CN-as was heated at 2 °C min^{-1} rate up to the desired temperature: 620 °C, 650 °C, 680 °C and 700 °C. The sample was maintained at the final temperature for 2 h before it was allowed to naturally cool-down to ambient temperature. Throughout the thermal treatment, the furnace was continuously purged with 50 mL min^{-1} of N_2. The thermally treated samples are referred to as 'CN-[temperature]', i.e. CN-700 for the material treated at 700 °C. The final mass of sample

CN-650 was 1.17 g, and 83 mg in the case of CN-700.

2.3 Characterization

Structural and chemical characterization Powder X-ray diffraction (PXRD) measurements were recorded at room temperature on a PANalytical X'Pert PRO diffractometer operating at 40 kV and 40 mA with monochromatized Cu Kα radiation (λ = 0.15418 nm). The materials' textural properties were obtained using a Micromeritics 3Flex apparatus. A two-stage degas process was employed to evacuate the samples from any adsorbate traces. During the first stage, a Micromeritics VacPrep Degasser was used to degas the samples, firstly at ambient temperature for about 5 h, followed by overnight degassing at 120 °C. The second stage consisted of an in situ degas performed at 120 °C for 5 h. The nitrogen adsorption and desorption isotherms were measured at 77 K. The Brunauer-Emmett-Teller (BET) surface area (S_{BET})[37] was calculated over the relative pressure range 0.05 to 0.35. The total pore volume (V_{Σ}) was calculated from the amount of nitrogen adsorbed at a relative pressure of about 0.97. The micropore volume (V_{μ}) was calculated by Dubinin-Radushkevich method.[38] Scanning electron microscopy (SEM) images were taken using a high resolution LEO Gemini 1525 FEGSEM at 5 kW in secondary electron mode (InLens detector). Prior to analysis, the samples were ground and mounted on carbon tape and coated with 10 nm chromium. Transmission electron microscopy (TEM) images were obtained using a JEOL 2100Plus instrument at an acceleration voltage of 200 kV. Before analysis, the samples were sonicated in ethanol and then drop casted on a carbon coated copper grid. Attenuated total reflection Fourier transform infrared (ATR-FTIR) spectra were collected at room temperature using a Perkin-Elmer Spectrum 100 Spectrometer equipped with and ATR cell. The spectra were generated, collected 8 times, and corrected for the background noise. The experiments were done on

powered samples, without KBr addition. X-ray photoelectron spectroscopy (XPS) measurements were carried out on a Thermo Scientific K-Alpha$^+$ X-ray Photoelectron Spectrometer equipped with a MXR3 Al Kα monochromated X-ray source (hν = 1486.6 eV). X-ray gun power was set to 72 W (6 mA and 12 kV). Survey scans were acquired using 200 eV pass energy, 0.5 eV step size and 100 ms (50 ms x 2 scans) dwell times. All high resolution spectra (C1s and N1s) were acquired using 20 eV pass energy, 0.1 eV step size. The samples were ground and mounted on the XPS sample holder using conductive carbon tape. Thermo Avantage was used for analysis of the XPS data with charging effects corrected by offsetting data so that the adventitious carbon occurred at 284.8 eV.

Optoelectronic properties characterization Diffuse reflectance ultraviolet-visible (DR-UV/Vis) spectra were obtained on an Agilent Cary 5000 UV-Vis-NIR equipped with an integrating sphere. The samples were compressed onto a KBr backed pellet for analysis. The spectral band width (SBW) was set to 2 nm and Spectralon was used as a standard. Chronoamperometry (CA) measurements were obtained using an Autolab PGSTAT302N electrochemical workstation, under cyclic irradiation (Δt = 20 s) from a Xe arc lamp (300 W, $\lambda > 325$ nm, LOT Quantum Design). The photo-current measurements were performed in a conventional three-electrode cell, using Pt and Ag/AgCl as the counter electrode and reference electrode, respectively. A voltage bias of 0.5 V was applied throughout the experiments. The working electrode was prepared on a fluorinedoped tin oxide (FTO) glass protected with the resin. The samples were dispersed in and sonicated in ethanol. The slurry was then deposited onto the FTO glass and dried at 65 °C. The electrolyte solution consisted of sodium sulfate with a concentration of 0.5 mol L^{-1}. Static photoluminescence (s-PL) measurements were obtained on a Fluorolog FM-32 spectrofluorometer (Horiba Jobin Yvon) in air with a visible detector. Diffuse reflectance transient

spectroscopy (DR-TS) measurements for the microsecond-second transient absorption decays were recorded using laser excitation pulses (6 ns) generated from a tunable optical parametric oscillator (Opolette 355, when the excitation λ was 355 nm). A liquid light guide with a diameter of 0.5 cm was used to transmit the laser pulse to the sample. The excitation density was typically adjusted to 170 µJ cm^{-2}, unless otherwise stated. A quartz halogen lamp (100 W, Bentham, IL 1) with a stabilized power supply (Bentham, 605) was used as the probe light source. To reduce stray light, scattered light, and sample emission, a monochromator was placed after the sample and appropriate light band pass filters were placed before the sample. The probe light passing through the sample was detected using a Si photodiode. The signal was passed through an amplifier (Costronics Electronics) and then measured using a digital oscilloscope (Tektronix 3012). The data was processed using home-built software based on Labview. The decays observed are the average between 16 and 32 averages laser pulses. For measurements in liquid phase, deionized water and 10 % TEOA aqueous solution were used. On gas phase measurements, air and Ar atmospheres were employed on the sample cell. In all cases the samples were degassed with Ar prior to measurements and then allowed to equilibrate for 2 min under the set-up conditions.

2.4 Photocatalytic H_2 evolution

A purpose-built liquid/solid teflon-lined reactor setup was assembled as illustrated in Figure S1. The photocatalyst (40 mg) was dispersed in 50 mL of 10 % TEOA aqueous solution and placed in a Teflon vessel. The vessel was inserted in a stainless steel closed reactor. Zero grade (99.998 %) N_2 was flowed at controlled rates using mass flow controllers (Omega Engineering, 0 to 100 mL min^{-1}). The system was purged with N_2 for 30 min and then H_2PtCl_6 solution was added in the amount correspondent to a mass frac-

tion of 2 % (Pt was used to serve as co-catalyst). The photo-reactor was vacuumed and replenished with N_2 five times. A Xe arc lamp (150 W, $\lambda > 325$ nm, LOT Quantum Design), equipped with a water filter was used as the irradiation source. When only visible radiation was used, a cut-off filter of 400 nm was employed. Under on-line operation, a continuous stream of 15 mL min^{-1} of N_2 purged the evolved gases from the reactor. Under semi-batch operation, the reactor was pressurized up to 1.28 bara, with samples collected every 1.5 h, up to 5 h. Evolved gases were detected using a gas chromatograph (Agilent Technologies) with hayesep and mol sieve columns in series, thermal conductivity and flame ionization detectors.

2.5 CO_2 adsorption and CO_2 photo-reduction

CO_2 sorption isotherms 25 °C were measured up to 1 bara using the 3Flex Micromeritics sorption analyzer. The same degas procedure was conducted as for N_2 sorption analyses. CO_2 photo-reduction was performed using a purpose-built gas/solid photo-reactor (Figure S2). The reactor internals accommodated a dry stage where the photocatalysts could be supported. The photocatalysts (25 mg) with added 2 % Pt on a mass basis were deposited on a stainless steel disk with a fixed area of 9.6 cm^2. Research grade (99.999 %) CO_2 and H_2 (99.9995 %, Peak Scientific PH200 hydrogen generator) were flown at controlled rates using mass flow controllers (Omega Engineering, 0 to 50 mL min^{-1}). Firstly, the photo-reactor was vacuumed and replenished with CO_2 and H_2 five times. Then, CO_2 and H_2 (1.5 vol/vol ratio) was passed over the photocatalyst bed in the photo-reactor for 15 residence times before it was sealed at 1.15 bara. A Xe arc lamp (150 W, $\lambda > 325$ nm, LOT Quantum Design) irradiated the photo-reactor with a single sample collected after 6 h of operation. The gas phase was analyzed with the previously described GC.

3 Results and Discussion

3.1 Materials characterization

Physical properties Structural characterization of the samples was first conducted in order to get insights into the effect of the thermal treatment on the morphology of the samples from the nano to the macroscale. The PXRD patterns of the as-synthesized and all the thermally treated g-C_3N_4 are shown in Figure 1a. Two main angle reflections are identified. The low-angle peak, at 13.0° ($d = 6.80$ Å) for the (100) reflection, can be attributed to the in-plane structural packing motif of the tri-s-triazine units while the strong peak, at around 27° for (002), corresponds to the inter-planar distance between sheets.[39] Figure 1b contains peak data obtained from the PXRD spectra. The results suggest an improved stacking of the g-C_3N_4 nanosheets, with the calculated inter-planar distance continuously decreasing from 3.25 Å to 3.18 Å, as the thermal treatment temperature increased from 560 °C to 700 °C. This trend has been previously reported[40,41] and is explained by a planarization of the single layers, as opposed to the potentially undulated bulk CN-as. This is further supported by the analysis of the full-width at half-maximum (FWHM) which shows a decrease of the peak widths as the thermal treatment temperature increases, suggesting again an improved stacking of the material's nanosheets. Hence, it is hypothesized that as the temperature of thermal treatment increases, the material's nanosheets are allowed to relax any non-planar imperfections, allowing for better packing. Interestingly, this is different from the distortion of the nanosheets upon thermal etching, that was observed by Chen et al.[32] – though PXRD patterns were not collected. We also note that in our work, we do not observe the pronounced amorphization that is apparent in other works from PXRD patterns, like for instance, the studies by Kang et al.[33] and Niu et al.[34] This could originate from the different synthesis precursor and conditions

applied in the post-thermal treatment.

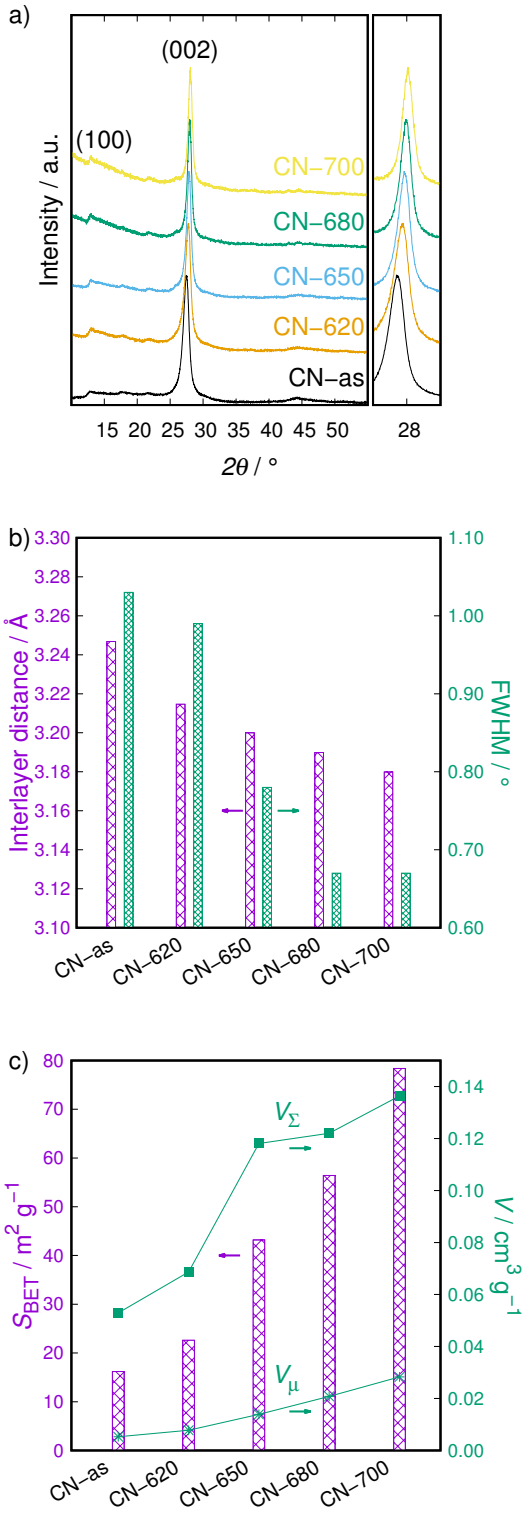

Figure 1: Characterization of the physical properties of the thermally-treated g-C_3N_4 samples: a) Powder X-ray diffraction patterns, right inset shows zoom over reflection (002) which corresponds to the layer stacking; b) Interlayer distance between g-C_3N_4 nanosheets and FWHM of reflection (002) of the powder X-ray diffraction; c) BET surface area, total pore volume (V_Σ) and micropore volume (V_μ).

To get further insight into the structure of the samples at the nanoscale, their porosity was analyzed using N_2 sorption isotherms at 77 K (Figure S3). The BET specific surface area increases more than four times up to 78.4 $m\,g^{-2}$, from CN-as to the highest thermally treated sample at 700 °C. The pore volumes and pore size distribution followed a similar trend with an increase in pore volume (Figure 1c, Figure S4). The increase in porosity and surface area is key in providing access to catalytic sites and reducing bulk charge recombination. We note that the increase in the BET surface area seems contradictory to the simultaneous decrease in the interlayer spacing observed earlier. We attribute this effect to the fact that the thermal treatment likely causes an increase in the amount of defects on the polymeric structure and particularly, triggers the formation of holes within the carbon nitride sheets structure thereby leading to an increase in porosity, as supported later via imaging. This has already been suggested in prior studies.[33,34]

SEM image provided some insight into the effect of the thermal treatment on the samples' morphology at the macroscale. CN-as (Figure 2a) exhibits a lumpy surface with no visible macropores. As the sample is subjected to thermal treatment, 'cracks' start appearing on the surface of samples (Figure 2b) and macropores become visible for the sample treated at the highest temperature (Figure 2c). TEM images are shown in Figure 2d-f. As observed in other studies,[33,34] the number/size of holes on the carbon nitride nanosheets increases with the extent of the thermal treatment.

To summarize, the physical properties of the g-C_3N_4 samples were dramatically modified by the thermal treatment. The porosity of the material increased considerably in micro-, meso- and macroscale regions, due to the appearances of defects/holes within the structure. In parallel, improved stacking of the nanosheets is indirectly observed.

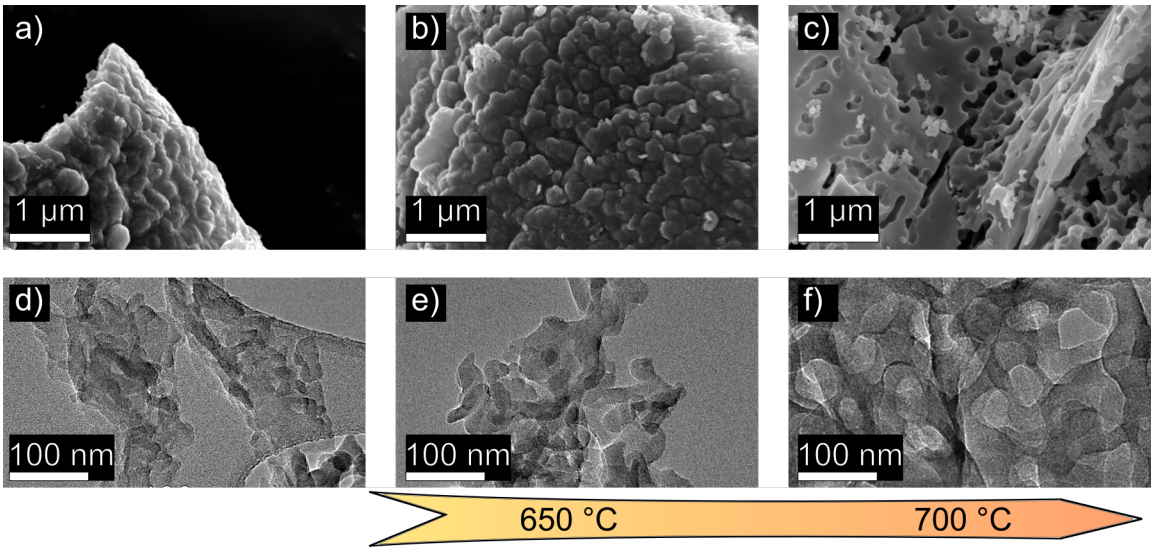

Figure 2: Characterization of the morphology of the thermally-treated g-C_3N_4 samples: SEM and TEM images of CN-as (a, d), CN-650 (b, e) and CN-700 (c,f).

Chemical properties In addition to the structure of the samples, the chemistry plays a role in the photocatalytic behavior of the materials. Material's surface chemistry can influence the adsorption behavior as well as the optoelectronic properties. Hence, XPS was employed to investigate possible chemical changes. As expected, the only observed species on the samples were C, N and O (Figure S5a). The XPS spectra were corrected for charging effects using adventitious carbon peak (284.8 eV) as reference.[34,42] The core levels of C (Figure 3a) were de-convoluted into three peaks (excluding adventitious carbon).[32,43,44] The main core level peak at 288.2 eV is ascribed to sp^2 hybridized carbon ($C-(N)_3$) of the tri-s-triazine rings.[45,46] The weaker peaks at 285.7 eV (O−C=O) and 288.7 eV (C−O) are due to surface oxidation of the carbon film.[42] Regarding the N core levels (Figure 3b), three peaks were found at 398.8 eV, 400.1 eV and 401.2 eV, which is attributed to sp^2 hybridized aromatic N atoms present in C−N=C, sp^3 hybridized N atoms in $N-(C)_3$ and terminal amino groups ($C-NH_2$ or =NH), respectively.[39,47] As expected, analysis of the nitrogen relative amounts (Figure 3c) shows a relative enrichment of car-

bon on the samples.[33–35] Indeed, as nitrogen leaves the g-C_3N_4 structure and gives origin to vacancies, the atomic ratio of C/N increases from 0.73 to 0.76.

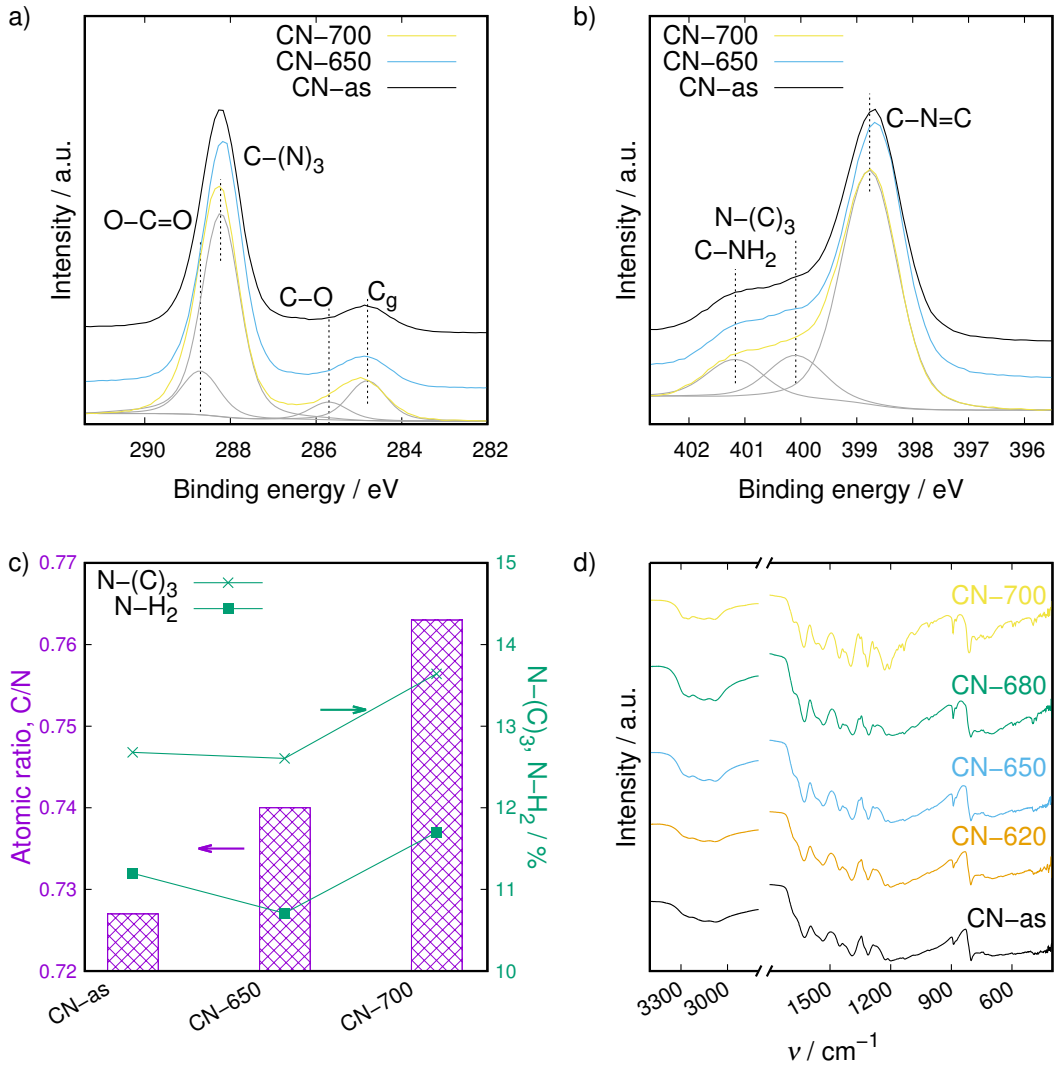

Figure 3: Characterization of the chemical properties of the thermally-treated g-C_3N_4: a) C core level XPS spectra; b) N core level XPS spectra; c) Relative amounts of different N species derived from the XPS spectra; d) ATR-FTIR spectra.

The ATR-FTIR spectra of the parent g-C_3N_4 and thermally treated materials are shown in Figure 3d. The sharp band at 800 cm^{-1} is characteristic of tri-s-triazine vibrations within the structures.[21,48] The multiple bands found between 1200 cm^{-1} and

1800 cm^{-1} are typical of C−N stretching and bending vibrations of N heterocycles.[39,49] No bands were observed between 1800 cm^{-1} and 3000 cm^{-1}, indicating that there are no triple-bonded −C≡N groups or double bonds −CN=C=C− in the g-C_3N_4 samples,[49] in accordance with the XPS data. Bands observed in the 3200 cm^{-1} region are due to N−H groups, at the edges of the tri-s-triazine units.[43,50] As the temperature of the thermal treatment increases, the bands intensity in that region increases due to the formation of defects and holes on the nanosheets structure and consecutive generation of more amino groups, as supported by the XPS data. This is in agreement with the findings from N_2 sorption.

Overall, the post-synthesis thermal treatment promotes the relative enrichment of carbon on the samples due to nitrogen being released from the g-C_3N_4 structure. These nitrogen vacancies are likely to play a role in the optoelectronic properties of the material.[32–35] Hence, a detailed study of the optoelectronic properties and photocatalytic performance was performed and is provided below.

Optoelectronic properties Finally, the optoelectronic properties of the materials were characterized as they are directly relevant to the photocatalytic performance. The steady state DR-UV/Vis spectra of the different samples are shown on Figure 4a. The parent material CN-as exhibits a single light absorption edge (not maxima) at around 450 nm. This absorption peak is characteristic of g-C_3N_4 polymers, and corresponds to the intrinsic electronic transition $\pi \rightarrow \pi^*$.[43] After thermal treatment at 620 °C, a red-shift of this sample's absorption edge is observed, in contrast to thermal treatments at higher temperatures which suffered a blue-shift of the same absorption peak. This behavior has previously been reported[26,32,51] and is a result of quantum confinement, due to the overall layer dimension reduction caused by breakage during thermal treatment.[52,53] In addition,

all thermally treated samples started developing a new absorption peak with an absorption edge (not maxima) at around 600 nm. This absorption peak becomes stronger as the temperature of the thermal treatment increases, being widely dominant on sample CN-700. This peak indicates the occurrence of n $\rightarrow \pi^*$ transitions for electrons available on the lone pairs of nitrogen present in tri-s-triazine.[32,43,49] Because such transitions are generally forbidden for perfectly symmetric tri-s-triazine planar units, the latter observation suggests the presence of structural distortions and defects generated during the thermal treatment, as supported by the materials' characterization analyzes discussed earlier.[49,54]

Next, we built a relative band diagram of selected materials (Figure 4b). This was done following the method used by Wang et al.[55] and Scanlon et al.[56] by using data from the XPS valence band and core levels positions, and the band gap energies obtained from DR-UV/Vis spectroscopy (Figure S6). Such approach relies only on experimental data and therefore avoid the need to make assumptions and/or simplification of the materials structure and chemistry that is required for theoretical studies. As seen in Figure 4b, as the temperature of the thermal treatment increases, the band gap of the materials is decreased resulting in a red-shift for the absorption of the materials. This is due to the shift of the conduction band to lower energies, likely caused by the introduction of N vacancies. On the other hand, the valence band position remains relatively unaltered after the thermal treatment. Moreover, materials CN-650 and CN-700 show an intermediate mid-gap state (inexistent for parent material CN-as), a direct result of transitions n $\rightarrow \pi^*$ now being allowed.[32] The position of the mid-gap state is covered later in this study.

Static photoluminescence (s-PL) spectra for the different samples were obtained and are presented in Figure 4c. Sample CN-as shows the most pronounced radiative recombination extent from all samples, as observed in other works.[33–35] The extent of occurring

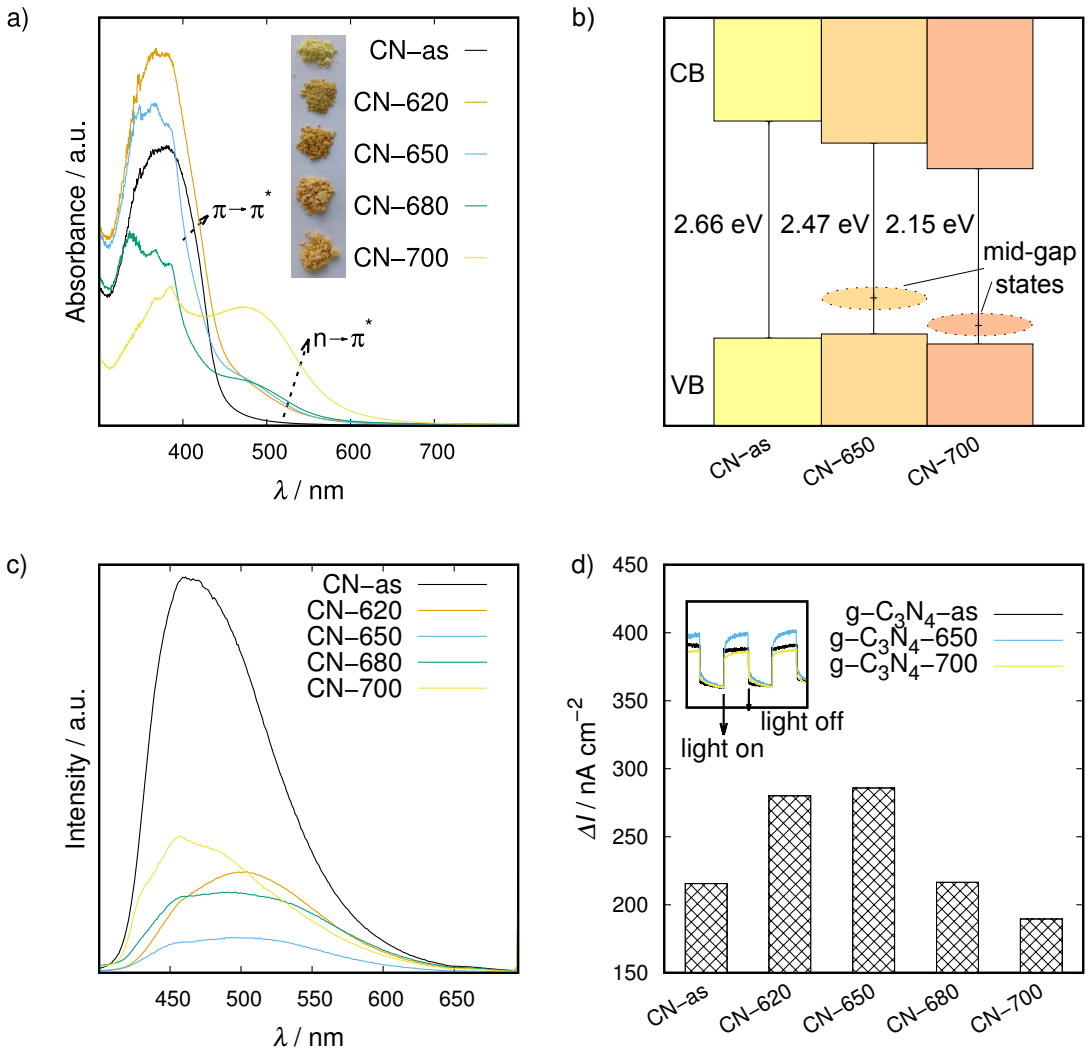

Figure 4: Characterization of the optoelectronic properties of the thermally-treated g-C_3N_4: a) DR-UV/Vis absorbance spectra; b) Band diagram for materials CN-as, CN-650 and CN-700; c) Static photoluminescence spectra; d) Photocurrent obtained by chronoamperometry with inset showing an extract of the raw signal.

fluorescence quenching is greatly decreased upon post-thermal treatment, with CN-650 exhibiting the least radiative recombination amount. A possible explanation for the immediate change of the radiative charge recombination may be due to the retention effects of trap states due to N vacancies, which can promote assisted recombination (as opposed

to band-to-band recombination) as well as the improved charge localization on more surface terminal sites.[33,34,57–59] Since g-C_3N_4 is a polymer with several tri-s-triazine units which constitute a conjugated network with the formation of π^* antibonding orbital, it is expected that the main emission s-PL peak emission is due to the electron-hole recombination from the excited charge and its corresponding hole.[32,60] CN-as photoluminescence emission maximum at 460 nm clearly matches the main valence band to conduction band excitation observed in the DR-UV/Vis spectra. For sample CN-620, the spectra is presented as a broad emission band with a maximum at around 500 nm.[49] In this case it is believed that charge recombination from trap states, mainly due to n $\rightarrow \pi^*$ electron transitions, start to have a significant impact on the spectra shape. As the thermal treatment temperature increases even further, samples show another emission peak at lower wavelengths. This secondary s-PL emission peak < 460 nm, can be attributed to new light absorption features shown on Figure 4a, that occur in the UV region, as observed for materials CN-650, CN-680 and CN-700.[32,61] Overall, it is expected that weaker s-PL peak emissions are a result of more efficient charge separation, which can potentially improve photocatalytic reactions.

Chronoamperometry (CA) measurements are shown on Figure 4d. The thermal treatment resulted in an increase in current up to 33 % for CN-650, when compared to parent material CN-as. Beyond 650 °C, the difference between the current in dark and under irradiation decreases, with CN-700 showing even lower current when compared with the parent material CN-as. Due to the nature of this experiment, it can be inferred that higher currents are due to higher oxidative reaction rates. This improved charge separation indicates that a photocatalyst is better able to more efficiently generate electron-hole species that can potentially participate in reactions.[46,47]

3.2 Photocatalytic activity

H_2 evolution The results for H_2 evolution are shown in Figure 5. As seen on Figure 5a, among the thermally treated g-C_3N_4 materials, CN-650 shows the best performance under flow operation using UV-vis light (77 % higher rate than CN-as). In general, the thermally treated samples show improved H_2 evolution compared to the parent material CN-as with the exception of sample CN-700. The trend is similar to that observed with the CA measurements (Figure 4d). Overall, the material's charge separation properties due to the existence of trap states, lead to a greater photocatalytic activity. Under visible light irradiation only (Figure 5b), CN-650 demonstrates again the highest H_2 evolution rates among the thermally treated samples. The other g-C_3N_4 thermally treated samples followed a similar trend to that observed under flow/UV-vis conditions with the exception of sample CN-700 which performed slightly better than CN-as. From these observations, it is suggested that the light absorption properties in relation to n $\rightarrow$ π^* transitions referred to earlier, have impacted the materials' H_2 evolution performance. As a result, CN-700 performs better than CN-as under visible light irradiation, despite worse charge separation capabilities based on CA.

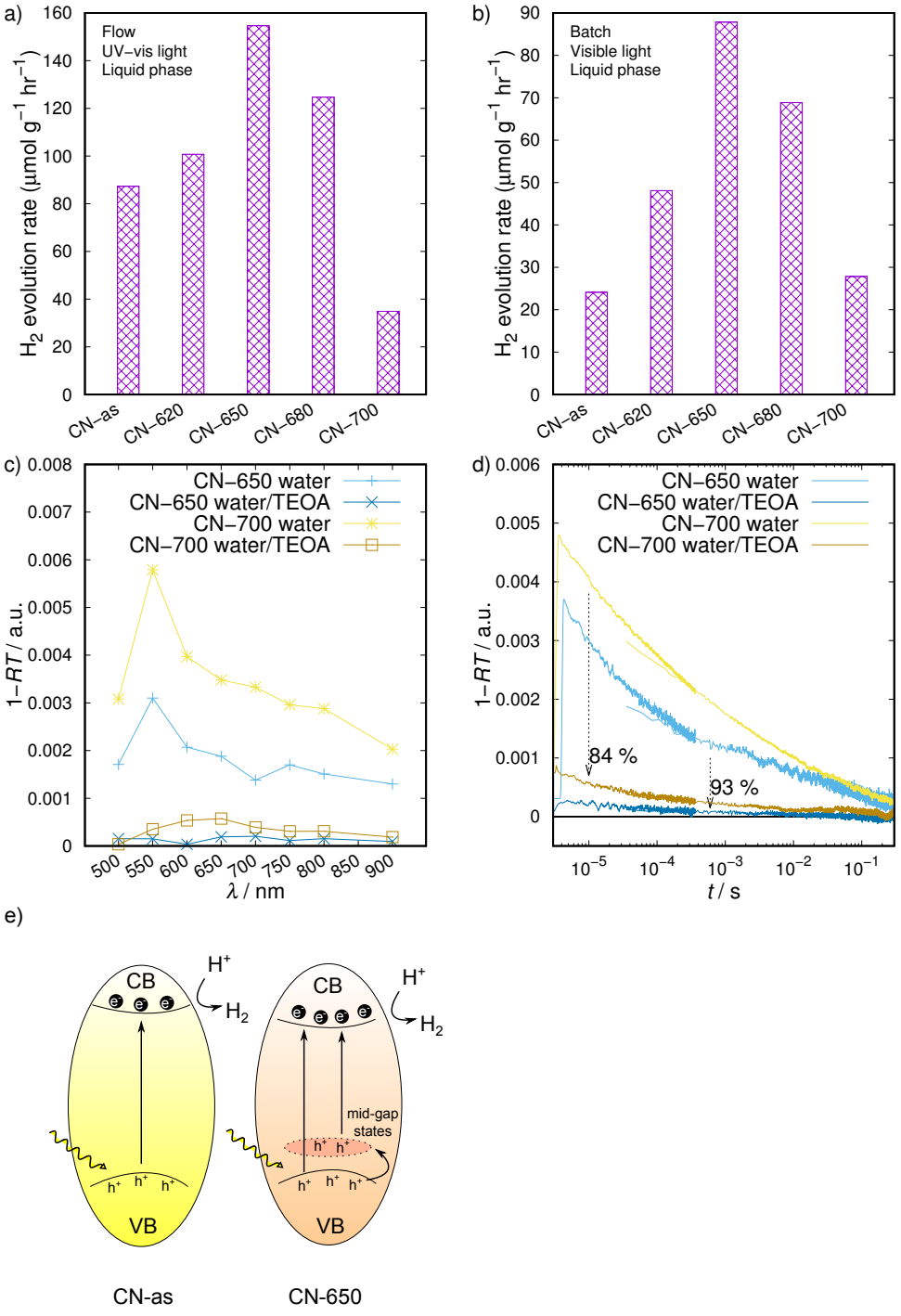

Figure 5: Photocatalytic evolution rate of H_2 produced in the photo-reactor under: a) flow operation and UV-visible light irradiation; b) Batch operation and visible light irradiation ($\geq$ 400 nm); Diffuse reflectance transient spectroscopy spectra: c) Dispersions of 1 mg mL^{-1} of CN-650 and CN-700 excited by a 100 µs pulsed excitation in the presence of water or 10 % by volume TEOA; d) Decay kinetics of CN-650 and CN-700 dispersions 1 mg mL^{-1} in water and TEOA aqueous solution monitored at 800 nm and excited by pulsed 355 nm excitation; e) Schematic of charge transfer for CN-as and CN-650, for H_2 evolution.

To gain a better understanding of the charge dynamics of the materials, DR-TS experiments on the annealed samples CN-650 and CN-700 were conducted in aqueous suspension, with and without the presence of a sacrificial agent, namely TEOA. In the latter case, as seen in Figure 5b, both materials are able to accumulate charges in water. However, the lack of H_2 evolution under these conditions, suggest that the observed species correspond to localized charges on defect states (or trap states). Interestingly, when the same experiments are carried out in the presence of TEOA, which is able to irreversibly react with the photo-generated holes, the amplitude of the spectra significantly decreases and the shape changes. This suggests that the accumulated charges in the absence of TEOA, were holes able to react with TEOA but not with water alone. These could be tentatively assigned to holes on the middle band states close to the valence band (see Figure 4b for the position of the mid-gap states) that can only be scavenged in the presence of a suitable sacrificial agent. We note that the position of these mid-gap states differs from those proposed in other studies,[34,35] which located them closer to the conduction band. In this report, the position of the mid-gap states was speculated to originate from the defects caused by the thermal treatment. Its position was assumed to be similar to that of the energy levels originated by the defects, which allowed for the $n \rightarrow \pi^*$ transitions. This is supported by the DR-TS results, where the holes trapped in the mid-gap states would to be located at an high enough potential to scavenge electrons from TEOA. Unfortunately, a direct quantitative comparison between the samples was impossible, due to the different suspension properties of the studied materials. Nevertheless, a quantitative interpretation of the results within each sample is achievable by analyzing the amount of charges under different conditions, i.e. with and without TEOA. The difference in signal amplitude between both conditions is due to the number of charges that have reacted with TEOA and correlate to how many electrons have survived long enough to gener-

ate H_2. These numbers are presented in (Figure 5d) and as can be observed, CN-650 is reacting with TEOA more efficiently (93 % signal reduction) than CN-700 (only 84 % of signal reduction), which translated into higher H_2 generation rates for sample CN-650. In summary, the obtained catalytic and spectroscopic results suggest that H_2 evolution is controlled by the material's charge formation abilities and light absorption capabilities. Based on the understanding of the charge transfer between electronic states, a schematic of the proposed mechanism is shown on Figure 5e.

CO_2 photo-reduction reaction We now focus our attention on the CO_2 photo-reduction experiments. As seen on Figure 6a, CO_2 uptake at 1 bar and 298 K (left hand side axis) increases with the thermal treatment, up to about 4 times for CN-680 and CN-700. This can be linked to the increase of N vacancies with the thermal treatment. The tested materials can be classified into two series by comparing the CO_2 uptake capacity with the catalytic activity (Figure 6a). Materials with low or moderate CO_2 uptake presented low CO_2 conversion while materials with high CO_2 uptake, namely CN-680 and CN-700, presented higher photoactivity. We speculate that the N vacancies are acting as not only the adsorption but also the reduction sites for CO_2. While the CO_2 uptake follows that of the porosity, it is unlikely that this was the governing factor for CO_2 photo-reduction at this low pressure. Instead, the creation of defects and the formation of amino groups (Figure 3c) is more likely to have played a role.

Interestingly, the trends in performance for H_2 evolution and CO_2 photo-reduction differ. In the latter case, enhancement when compared to the reference material, CN-as, is only observed at the highest temperatures, i.e. 680 °C and 700 °C, with CN-700 sample exhibiting a CO production rate 1.7 times higher than that of CN-as. This behavior highlights the intrinsically different mechanisms taking place for the two reactions and

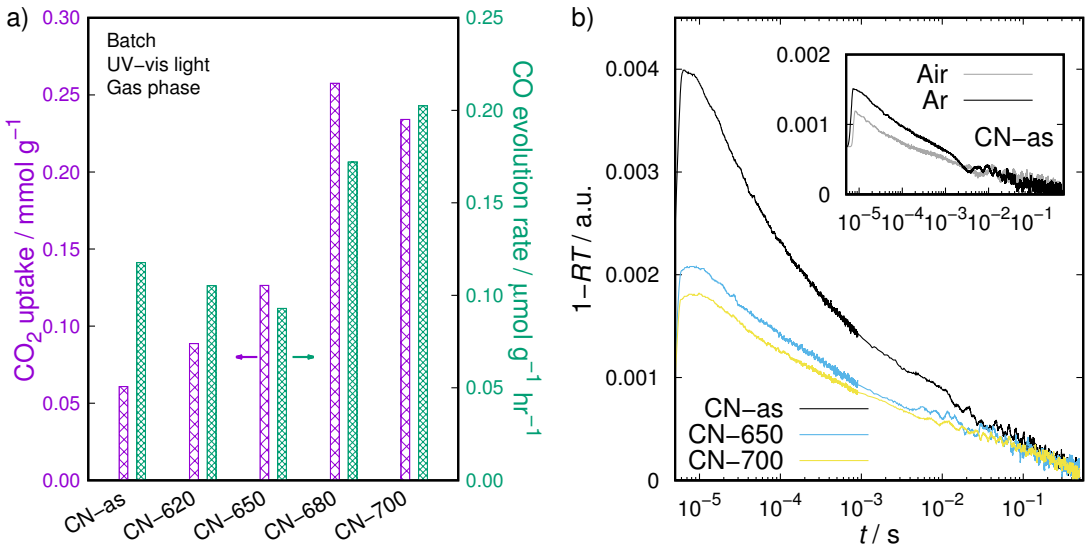

Figure 6: a) Left axis: CO_2 uptake at 1 bar, 298 K. Right axis: Photocatalytic evolution of CO, as a result of a reaction of CO_2 reduction, under batch conditions in gas phase and UV-visible light irradiation; b) Decay kinetics in Ar monitored at 800 nm and excited by pulsed 355 nm excitation, inset shows decay kinetics of sample CN-as in air and Ar.

points to the different materials requirements. We note that Tu et al.[35] recently reported that the most active post-thermally treated g-C_3N_4 for H_2 evolution also presented the highest CO_2 photo-reduction rates. This differs from our findings. We attribute this to the different materials' features caused by the distinct thermal treatment conditions, in terms of temperature and atmosphere. In fact, this difference supports our hypothesis that the materials 'profile' directly influence its photocatalytic properties.

In order to rationalize these results, analogous DR-TS experiments to those conducted to understand H_2 evolution, were performed in gas phase (Figure 6b) under Ar (inert conditions) and air (the O_2 present in this conditions can react with the accumulated electrons). Firstly, it is noted that very different spectral features are observed for each sample in gas phase (Figure S7, when directly compared to the liquid phase DR-TS experiments), a distinction that is also observed on the CO_2 photo-reduction experiments (Figure 6a). This suggests that the environment of the material impacts the nature of

the trap states (long lived), resulting in different spectral features. Under inert conditions (Ar atmosphere), all the observed charges at long time scales are assigned to trap states. When the experiment was carried out under the same light conditions, CN-as was the one presenting more trapped charges, with CN-650 and CN-700 showing a similar number of trap charges. Quenching experiments using O_2 as electron scavenger (inset Figure 6b), suggest that the charges accumulated on CN-as are more reactive towards O_2 in comparison to samples CN-650 or CN-700, which presented unaltered spectra and kinetics. This indicates that the charges observed under Ar atmosphere for CN-as are reactive towards reduction reactions. This is in agreement with the higher CO_2 photo-reduction rates observed for this material when compared to CN-650, despite CN-as presenting lower CO_2 uptake (Figure 6a). These results might seem contradictory to those obtained using s-PL and CA, which pointed to a higher extent of radiative recombination and lower charge separation in CN-as. However, one should note that DR-TS delivers time-resolved results and is able to screen for details that are only 'averaged out' by the other techniques. At higher thermal treatment temperatures, comparing CN-650 and CN-700 performance, DR-TS data cannot explain the trend observed in terms of CO production. In that case, it appears that CO_2 photo-reduction activity is controlled not by defect states linked to charge recombination, but mostly by the CO_2 adsorption ability. In this instance, materials with the highest CO_2 uptake show the highest CO_2 photo-reduction rates from all materials, highlighting the importance of this property.

Conclusions

Thermal treatment of g-C_3N_4 is shown to impact the physical, chemical and optoelectronic properties of the materials in a tunable manner. In particular, we note the creation of N vacancies and defects/holes within the nanosheets which leads to an enhanced porosity.

These variations induce changes in the optoelectronic properties of the materials: (i) appearance of n $\rightarrow \pi^*$ transitions, (ii) red-shift in the light absorption, and (iii) improved charge separation and reduced charge recombination. The latter aspect is linked to the presence of trap states, which we 'locate' close to the valence band.

These combined material features promote the photocatalytic performance for both H_2 evolution and CO_2 photo-reduction. Yet, the relative importance of these features varies depending on the reaction considered. We show that H_2 evolution is mainly governed by the light absorption properties of the materials and their intrinsic charge formation. On the other hand, CO_2 photo-reduction (conducted in a gas-solid reactor) is favored by either the presence of long-lived trapped charges in the case of the untreated sample or by the enhanced CO_2 uptake for the thermally treated samples which exhibit higher porosity and amine functionalization.

Acknowledgments

This work was supported by the Engineering and Physical Sciences Research Council (EP/1508320) and the EU for a Marie Curie fellowship (658270). The authors would also acknowledge the support from the Department of Chemical Engineering at Imperial College London.

Supporting Information

The following files are available free of charge.

- SI.pdf: Hole scavenging calculations and additional figures

References

(1) Bolton, J. R. Solar Fuels. *Science* **1978**, *202*, 705–711.

(2) Roy, S. C.; Varghese, O. K.; Paulose, M.; Grimes, C. A. Toward Solar Fuels: Photocatalytic Conversion of Carbon Dioxide to Hydrocarbons. *ACS Nano* **2010**, *4*, 1259–1278.

(3) Ismail, A. A.; Bahnemann, D. W. Photochemical splitting of water for hydrogen production by photocatalysis: A review. *Sol. Energy Mater. Sol. Cells* **2014**, *128*, 85–101.

(4) Chen, X.; Shen, S.; Guo, L.; Mao, S. S. Semiconductor-based Photocatalytic Hydrogen Generation. *Chem. Rev.* **2010**, *110*, 6503–6570.

(5) Gust, D.; Moore, T. A.; Moore, A. L. Solar Fuels via Artificial Photosynthesis. *Acc. Chem. Res.* **2009**, *42*, 1890–1898.

(6) Liu, G.; Hoivik, N.; Wang, K.; Jakobsen, H. Engineering TiO_2 nanomaterials for CO_2 conversion/solar fuels. *Sol. Energy Mater. Sol. Cells* **2012**, *105*, 53–68.

(7) Ge, M.; Cai, J.; Iocozzia, J.; Cao, C.; Huang, J.; Zhang, X.; Shen, J.; Wang, S.; Zhang, S.; Zhang, K.-Q.; Lai, Y.; Lin, Z. A review of TiO_2 nanostructured catalysts for sustainable H_2 generation. *Int. J. Hydrogen Energy* **2017**, *42*, 8418–8449.

(8) Low, J.; Cheng, B.; Yu, J. Surface modification and enhanced photocatalytic CO_2 reduction performance of TiO_2 : a review. *Appl. Surf. Sci.* **2017**, *392*, 658–686.

(9) Smestad, G. P.; Steinfeld, A. Review: Photochemical and Thermochemical Production of Solar Fuels from H_2O and CO_2 Using Metal Oxide Catalysts. *Ind. Eng. Chem. Res.* **2012**, *51*, 11828–11840.

(10) Montoya, J. H.; Seitz, L. C.; Chakthranont, P.; Vojvodic, A.; Jaramillo, T. F.; Nørskov, J. K. Materials for solar fuels and chemicals. *Nat. Mater.* **2017**, *16*, 70–81.

(11) Xiang, Q.; Cheng, B.; Yu, J. Graphene-Based Photocatalysts for Solar-Fuel Generation. *Angew. Chem. Int. Ed.* **2015**, *54*, 11350–11366.

(12) Samanta, S.; Martha, S.; Parida, K. Facile Synthesis of Au/g-C_3N_4 Nanocomposites: An Inorganic/Organic Hybrid Plasmonic Photocatalyst with Enhanced Hydrogen Gas Evolution Under Visible-Light Irradiation. *ChemCatChem* **2014**, 1453–1462.

(13) Ge, L.; Han, C.; Xiao, X.; Guo, L. Synthesis and characterization of composite visible light active photocatalysts MoS_2–g-C_3N_4 with enhanced hydrogen evolution activity. *Int. J. Hydrogen Energy* **2013**, *38*, 6960–6969.

(14) An, C.; Wang, J.; Jiang, W.; Zhang, M.; Ming, X.; Wang, S.; Zhang, Q. Strongly visible-light responsive plasmonic shaped AgX:Ag (X = Cl, Br) nanoparticles for reduction of CO_2 to methanol. *Nanoscale* **2012**, *4*, 5646.

(15) Tahir, M.; Tahir, B.; Amin, N. A. S. Gold-nanoparticle-modified TiO_2 nanowires for plasmon-enhanced photocatalytic CO_2 reduction with H_2 under visible light irradiation. *Appl. Surf. Sci.* **2015**, *356*, 1289–1299.

(16) Dias, E. M.; Petit, C. Towards the use of metal-organic frameworks for water reuse: a review of the recent advances in the field of organic pollutants removal and degradation and the next steps in the field. *J. Mater. Chem. A* **2015**, *3*, 22484–22506.

(17) Crake, A. Metal-organic frameworks based materials for photocatalytic CO_2 reduction. *Mater. Sci. Technol.* **2017**, *33*, 1737–1749.

(18) Ong, W.-J.; Tan, L.-L.; Ng, Y. H.; Yong, S.-T.; Chai, S.-P. Graphitic Carbon Nitride (g-C_3N_4)-Based Photocatalysts for Artificial Photosynthesis and Environmental Remediation: Are We a Step Closer To Achieving Sustainability? *Chem. Rev.* **2016**, *116*, PMID: 27199146, 7159–7329.

(19) Cao, S.; Low, J.; Yu, J.; Jaroniec, M. Polymeric Photocatalysts Based on Graphitic Carbon Nitride. *Adv. Mater.* **2015**, *27*, 2150–2176.

(20) Zhao, Z.; Sun, Y.; Dong, F. Graphitic carbon nitride based nanocomposites: a review. *Nanoscale* **2015**, *7*, 15–37.

(21) Jürgens, B.; Irran, E.; Senker, J.; Kroll, P.; Müller, H.; Schnick, W. Melem (2,5,8-Triamino-tri-s-triazine), an Important Intermediate during Condensation of Melamine Rings to Graphitic Carbon Nitride: Synthesis, Structure Determination by X-ray Powder Diffractometry, Solid-State NMR, and Theoretical Studies. *J. Am. Chem. Soc.* **2003**, *125*, 10288–10300.

(22) Wang, Y.; Wang, X.; Antonietti, M. Polymeric Graphitic Carbon Nitride as a Heterogeneous Organocatalyst: From Photochemistry to Multipurpose Catalysis to Sustainable Chemistry. *Angew. Chem. Int. Ed.* **2011**, *51*, 68–89.

(23) Wang, X.; Blechert, S.; Antonietti, M. Polymeric Graphitic Carbon Nitride for Heterogeneous Photocatalysis. *ACS Catal.* **2012**, *2*, 1596–1606.

(24) Dong, F.; Zhao, Z.; Xiong, T.; Ni, Z.; Zhang, W.; Sun, Y.; Ho, W.-K. In Situ Construction of g-C_3N_4/g-C_3N_4 Metal-Free Heterojunction for Enhanced Visible-Light Photocatalysis. *ACS Appl. Mater. Interfaces* **2013**, *5*, PMID: 24144400, 11392–11401.

(25) Kumar, S.; Karthikeyan, S.; Lee, A. g-C_3N_4-Based Nanomaterials for Visible Light-Driven Photocatalysis. *Catalysts* **2018**, *8*, 74.

(26) Sun, J.; Zhang, J.; Zhang, M.; Antonietti, M.; Fu, X.; Wang, X. Bioinspired hollow semiconductor nanospheres as photosynthetic nanoparticles. *Nat. Commun.* **2012**, 1139.

(27) Wen, J.; Xie, J.; Chen, X.; Li, X. A review on g-C_3N_4-based photocatalysts. *Appl. Surf. Sci.* **2017**, *391, Part B*, 2nd International Symposium on Energy and Environmental Photocatalytic Materials, 72–123.

(28) Zhang, J.; Zhang, G.; Chen, X.; Lin, S.; Möhlmann, L.; Dolega, G.; Lipner, G.; Antonietti, M.; Blechert, S.; Wang, X. Co-Monomer Control of Carbon Nitride Semiconductors to Optimize Hydrogen Evolution with Visible Light. *Angew. Chem. Int. Ed.* **2012**, *51*, 3183–3187.

(29) Zhang, J.; Zhang, M.; Sun, R.-Q.; Wang, X. A Facile Band Alignment of Polymeric Carbon Nitride Semiconductors to Construct Isotype Heterojunctions. *Angew. Chem. Int. Ed.* **2012**, *51*, 10145–10149.

(30) Zhang, G.; Zhang, M.; Ye, X.; Qiu, X.; Lin, S.; Wang, X. Iodine Modified Carbon Nitride Semiconductors as Visible Light Photocatalysts for Hydrogen Evolution. *Adv. Mater.* **2013**, *26*, 805–809.

(31) Wang, X.; Chen, X.; Thomas, A.; Fu, X.; Antonietti, M. Metal-Containing Carbon Nitride Compounds: A New Functional Organic-Metal Hybrid Material. *Adv. Mater.* **2009**, *21*, 1609–1612.

(32) Chen, Y.; Wang, B.; Lin, S.; Zhang, Y.; Wang, X. Activation of $n \rightarrow \pi^*$ Transitions in Two-Dimensional Conjugated Polymers for Visible Light Photocatalysis. *J. Phys. Chem. C* **2014**, *118*, 29981–29989.

(33) Kang, Y.; Yang, Y.; Yin, L.-C.; Kang, X.; Wang, L.; Liu, G.; Cheng, H.-M. Selective Breaking of Hydrogen Bonds of Layered Carbon Nitride for Visible Light Photocatalysis. *Adv. Mater.* **2016**, *28*, 6471–6477.

(34) Niu, P.; Qiao, M.; Li, Y.; Huang, L.; Zhai, T. Distinctive defects engineering in graphitic carbon nitride for greatly extended visible light photocatalytic hydrogen evolution. *Nano Energy* **2018**, *44*, 73–81.

(35) Tu, W.; Xu, Y.; Wang, J.; Zhang, B.; Zhou, T.; Yin, S.; Wu, S.; Li, C.; Huang, Y.; Zhou, Y.; Zou, Z.; Robertson, J.; Kraft, M.; Xu, R. Investigating the Role of Tunable Nitrogen Vacancies in Graphitic Carbon Nitride Nanosheets for Efficient Visible-Light-Driven H_2 Evolution and CO_2 Reduction. *ACS Sustainable Chem. Eng.* **2017**, *5*, 7260–7268.

(36) Lin, L.; Ren, W.; Wang, C.; Asiri, A. M.; Zhang, J.; Wang, X. Crystalline carbon nitride semiconductors prepared at different temperatures for photocatalytic hydrogen production. *Appl. Catal., B* **2018**, *231*, 234–241.

(37) Brunauer, S.; Emmett, P. H.; Teller, E. Adsorption of Gases in Multimolecular Layers. *J. Am. Chem. Soc.* **1938**, *60*, 309–319.

(38) Nguyen, C. M.; Do, D. D. The Dubinin-Radushkevich equation and the underlying microscopic adsorption description. *Carbon* **2001**, *39*, 1327–1336.

(39) Ho, W.; Zhang, Z.; Xu, M.; Zhang, X.; Wang, X.; Huang, Y. Enhanced visible-light-driven photocatalytic removal of NO: Effect on layer distortion on g-C_3N_4 by H_2 heating. *Appl. Catal., B* **2015**, *179*, 106–112.

(40) Niu, P.; Zhang, L.; Liu, G.; Cheng, H.-M. Graphene-Like Carbon Nitride Nanosheets for Improved Photocatalytic Activities. *Adv. Funct. Mater.* **2012**, *22*, 4763–4770.

(41) Groenewolt, M.; Antonietti, M. Synthesis of g-C_3N_4 Nanoparticles in Mesoporous Silica Host Matrices. *Adv. Mater.* **2005**, *17*, 1789–1792.

(42) Miller, T. S.; Jorge, A. B.; Suter, T. M.; Sella, A.; Cora, F.; McMillan, P. F. Carbon nitrides: synthesis and characterization of a new class of functional materials. *Phys. Chem. Chem. Phys.* **2017**, *19*, 15613–15638.

(43) Khabashesku, V. N.; Zimmerman, J. L.; Margrave, J. L. Powder Synthesis and Characterization of Amorphous Carbon Nitride. *Chem. Mater.* **2000**, *12*, 3264–3270.

(44) Lu, X.; Xu, K.; Chen, P.; Jia, K.; Liu, S.; Wu, C. Facile one step method realizing scalable production of g-C_3N_4 nanosheets and study of their photocatalytic H_2 evolution activity. *J. Mater. Chem. A* **2014**, *2*, 18924–18928.

(45) Dementjev, A. P.; de Graaf, A.; van de Sanden, M. C. M.; Maslakov, K. I.; Naumkin, A. V.; Serov, A. A. X-Ray photoelectron spectroscopy reference data for identification of the C_3N_4 phase in carbon–nitrogen films. *Diamond Relat. Mater.* **2000**, *9*, 1904–1907.

(46) Zhang, Y.; Schnepp, Z.; Cao, J.; Ouyang, S.; Li, Y.; Ye, J.; Liu, S. Biopolymer-Activated Graphitic Carbon Nitride towards a Sustainable Photocathode Material. *Sci. Rep.* **2013**, *3*, DOI: 10.1038/srep02163.

(47) Chen, L.; Man, Y.; Chen, Z.; Zhang, Y. Ag/g-C_3N_4 layered composites with enhanced visible light photocatalytic performance. *Mater. Res. Express* **2016**, *3*, 115003.

(48) Kumar, S.; Surendar, T.; Kumar, B.; Baruah, A.; Shanker, V. Synthesis of highly efficient and recyclable visible-light responsive mesoporous g-C_3N_4 photocatalyst via facile template-free sonochemical route. *RSC Advances* **2014**, *4*, 8132.

(49) Jorge, A. B.; Martin, D. J.; Dhanoa, M. T. S.; Rahman, A. S.; Makwana, N.; Tang, J.; Sella, A.; Corà, F.; Firth, S.; Darr, J. A.; McMillan, P. F. H_2 and O_2 Evolution from Water Half-Splitting Reactions by Graphitic Carbon Nitride Materials. *J. Phys. Chem. C* **2013**, *117*, 7178–7185.

(50) Zhang, M.; Nakayama, Y. Effect of ultraviolet light irradiation on amorphous carbon nitride films. *J. Appl. Phys.* **1997**, *82*, 4912–4915.

(51) Zhang, X.; Xie, X.; Wang, H.; Zhang, J.; Pan, B.; Xie, Y. Enhanced Photoresponsive Ultrathin Graphitic-Phase C_3N_4 Nanosheets for Bioimaging. *J. Am. Chem. Soc.* **2013**, *135*, 18–21.

(52) Nirmal, M.; Dabbousi, B. O.; Bawendi, M. G.; Macklin, J. J.; Trautman, J. K.; Harris, T. D.; Brus, L. E. Fluorescence intermittency in single cadmium selenide nanocrystals. *Nature* **1996**, *383*, 802–804.

(53) Bai, J.; Zhong, X.; Jiang, S.; Huang, Y.; Duan, X. Graphene nanomesh. *Nat. Nanotechnol.* **2010**, *5*, 190–194.

(54) Deifallah, M.; McMillan, P. F.; Corà, F. Electronic and Structural Properties of Two-Dimensional Carbon Nitride Graphenes. *J. Phys. Chem. C* **2008**, *112*, 5447–5453.

(55) Wang, J.; Liu, X.-L.; Yang, A.-L.; Zheng, G.-L.; Yang, S.-Y.; Wei, H.-Y.; Zhu, Q.-S.; Wang, Z.-G. Measurement of wurtzite ZnO/rutile TiO_2 heterojunction band offsets by x-ray photoelectron spectroscopy. *Appl. Phys. A* **2010**, *103*, 1099–1103.

(56) Scanlon, D. O.; Dunnill, C. W.; Buckeridge, J.; Shevlin, S. A.; Logsdail, A. J.; Woodley, S. M.; Catlow, C. R. A.; Powell, M. J.; Palgrave, R. G.; Parkin, I. P.; Watson, G. W.; Keal, T. W.; Sherwood, P.; Walsh, A.; Sokol, A. A. Band alignment of rutile and anatase TiO_2. *Nat. Mater.* **2013**, *12*, 798–801.

(57) Wang, Y.; Zhang, J.; Wang, X.; Antonietti, M.; Li, H. Boron- and Fluorine-Containing Mesoporous Carbon Nitride Polymers: Metal-Free Catalysts for Cyclohexane Oxidation. *Angew. Chem. Int. Ed.* **2010**, *49*, 3356–3359.

(58) Niu, P.; Yin, L.-C.; Yang, Y.-Q.; Liu, G.; Cheng, H.-M. Increasing the Visible Light Absorption of Graphitic Carbon Nitride (Melon) Photocatalysts by Homogeneous Self-Modification with Nitrogen Vacancies. *Adv. Mater.* **2014**, *26*, 8046–8052.

(59) Yu, H.; Shi, R.; Zhao, Y.; Bian, T.; Zhao, Y.; Zhou, C.; Waterhouse, G. I. N.; Wu, L.-Z.; Tung, C.-H.; Zhang, T. Alkali-Assisted Synthesis of Nitrogen Deficient Graphitic Carbon Nitride with Tunable Band Structures for Efficient Visible-Light-Driven Hydrogen Evolution. *Adv. Mater.* **2017**, *29*, 1605148.

(60) Zhang, Y.; Pan, Q.; Chai, G.; Liang, M.; Dong, G.; Zhang, Q.; Qiu, J. Synthesis and luminescence mechanism of multicolor-emitting g-C_3N_4 nanopowders by low temperature thermal condensation of melamine. *Sci. Rep.* **2013**, *3*, DOI: `10.1038/srep01943`.

(61) Godin, R.; Wang, Y.; Zwijnenburg, M. A.; Tang, J.; Durrant, J. R. Time-Resolved Spectroscopic Investigation of Charge Trapping in Carbon Nitrides Photocatalysts for Hydrogen Generation. *J. Am. Chem. Soc.* **2017**, *139*, PMID: 28319382, 5216–5224.

Graphical TOC Entry